Chemical Science

ROYAL SOCIETY OF CHEMISTRY

EDGE ARTICLE

View Article Online
View Journal | View Issue

Cite this: *Chem. Sci.*, 2025, **16**, 20048

All publication charges for this article have been paid for by the Royal Society of Chemistry

An acceptor motor-driven electronic donor–acceptor supramolecular scaffold towards imaging-guided tumor therapy

Canze Zheng,†[a] Liwei Zhu,†[b] Jianyu Zhang,†[c] Xin Deng,[a] Zhengyao Zhong,[a] Xiang He,[a] Qiaoyun Zhang,[a] Junkai Liu,[d] Miao Meng,[a] Jacky W. Y. Lam,[d] Ying Li,*[b] Ming Chen*[a] and Ben Zhong Tang*[e]

Traditional approaches to accessing near infrared (NIR) photothermal agents mainly focus on synthesis methods. Herein, based on a supramolecular strategy, an electrostatic force-driven electronic donor–acceptor complex is established with 1,4,5,8,9,11-hexaazatriphenylenehexacarbonitrile (HAT-CN) and perylene as the acceptor and donor, respectively. Due to the strong electronic affinity of the acceptor and the opposite electronic properties between them, through-space charge transfer occurs in the assembly, markedly narrowing the energy gap, thereby inducing obvious NIR absorption and benefiting photothermal conversion. More interestingly, the bond stretching vibration is dramatic and sufficient in the acceptor, making it an acceptor motor in the supramolecular complex to further enhance the photothermal properties. As a result, a prompt heating effect by more than 190 °C can be obtained in the powder under 808 nm laser excitation and the photothermal conversion efficiency of the nanoparticles (NPs) reaches as high as 59.4%. Owing to the good photothermal effect, *in vitro* and *in vivo* photoacoustic (PA) imaging can be well performed with the NPs. Moreover, the NPs exhibit prominent phototoxicity to kill CT26 cells and ablate tumors in living mice with the photothermal immunomodulatory effect evoked concurrently. The synergetic strategy in this work provides a facile, economical and flexible avenue for designing highly efficient NIR photothermal agents to accelerate practical biomedical applications.

Received 31st July 2025
Accepted 15th September 2025

DOI: 10.1039/d5sc05770a

rsc.li/chemical-science

Introduction

Supramolecular chemistry is "the chemistry of intermolecular bonds, covering the structures and functions of the entities formed by association of two or more chemical species".[1,2] Non-covalent interactions play a significant role in the properties of supramolecular assemblies, which widely exist in the form of van der Waals, hydrogen bond, hydrophobic, electrostatic, metal-coordination or host–guest interactions.[3–10] Among the supramolecular assemblies, the aromatic donor–acceptor complexes formed as a result of an electrostatic force have drawn much attention over the past decades due to their promising optoelectronic properties.[11–16] In such a supramolecular system, charge transfer can occur in the space between the reorganized frontier molecular orbitals in the donor–acceptor complexes, thereby inducing potential functionalities such as ambipolar transport, metallicity, photoconductivity, and so forth, which are different from those of the individual components.[17–22] For example, the use of the tetrathiafulvalene-7,7,8,8-tetracyanoquinodimethane (TTF-TCNQ) charge-transfer complex has caused a drastic improvement in the electron mobility in an organic semiconductor compared with the devices with either silver or gold contacts.[23,24] Inspired by the interesting properties, many complexes have been established based on other donors (*e.g.* perylene, pyrene, *trans*-stilbene, *etc.*) or acceptors (*e.g.* tetracyanoethylene, 1,2,4,5-tetracyanobenzene, perylene bisimide, *etc.*) to expand their applications.[25–31] However, they still focus on electronic devices and adoptable donors or acceptors are limited, which has hampered their development.

[a]*College of Chemistry and Materials Science, Jinan University, Guangzhou 510632, China. E-mail: chenming@jnu.edu.cn*

[b]*Innovation Research Center for AIE Pharmaceutical Biology, School of Pharmaceutical Sciences and the Second Affiliated Hospital, Guangzhou Medical University, Guangzhou 511436, China. E-mail: liying@gzhmu.edu.cn*

[c]*MOE Key Laboratory of Macromolecular Synthesis and Functionalization, Department of Polymer Science and Engineering, Zhejiang University, Hangzhou 310058, China*

[d]*Department of Chemistry, Hong Kong Branch of Chinese National Engineering Research Center for Tissue Restoration and Reconstruction, Guangdong-Hong Kong-Macau Joint Laboratory of Optoelectronic and Magnetic Materials, The Hong Kong University of Science and Technology, Clear Way Bay, Kwoloon, Hong Kong, 999077, China*

[e]*Guangdong Basic Research Center of Excellence for Aggregate Science, School of Science and Engineering, The Chinese University of Hong Kong (Shenzhen), Longgang, Shenzhen, Guangdong 518172, China. E-mail: tangbenz@cuhk.edu.cn*

† These authors contributed equally to this work.

The use of organic materials for cancer imaging and phototherapy exhibits advantages such as good biocompatibility, high accuracy and resolution, low drug tolerance, negligible side effects, *etc.*[32–36] However, the low light permeability caused by light absorption from the biosubstance and light scattering from the tissue has hindered their applications. To address this issue, designing organic agents with near infrared (NIR) light excitations has emerged as a main task in this area.[37–42] The incorporation of strong electronic donors and acceptors into a molecular system may result in effective intramolecular or through-bond charge transfer to remarkably narrow the energy gap and red-shift the absorption.[43–46] However, the trivial molecular design and synthesis and the decreased processability caused by the increased molecular rigidity are not ignorable. Different from the above design viewpoint, through-space charge transfer often takes place in a donor–acceptor supramolecular complex formed by a physical interaction, which can serve as an attractive platform to develop NIR agents.[23] Apparently, this synthesis-free process may avoid the complicated preparation steps, and the materials can be generated readily during the self-assembly process, which avoids the enlarged molecular rigidity from the synthesis to decrease the processability. More importantly, free from the chemical bond limitation, the array and distance between the donors and acceptors are readily tunable to have a profound effect on their properties.[47–49] These features would provide huge opportunities to bridge donor–acceptor supramolecular complexes with biomedical applications.

The investigation of molecular motion in a molecular motor in the aggregate state is fascinating since it is commonly accepted that it is almost prohibited by the steric effect.[50–52] Especially for a nanoplatform constructed from molecular motors, it is vital to establish a relationship between the molecular motion and the photothermal conversion after light excitation as effective photothermal performance is crucial for biomedical applications. For example, the vigorous thermal-elastic expansion caused by heat formation from nanoagents under pulse laser excitation may enable photoacoustic (PA) imaging with a high spatial resolution and deep penetration depth.[53,54] Moreover, the generated heat can kill cancer cells and bacteria or affect the life process.[55,56] Up to now, many approaches such as introduction of a group rotator, adoption of bond stretching vibration, increasing the intermolecular gap by introducing the flexible side groups and manipulating the twisted intramolecular charge transfer effect have been adopted to promote molecular motion and photothermal conversion in molecular motors.[57–60] However, they have all been studied *via* intramolecular processes in single-molecule systems. On the other hand, electronic donor–acceptor supramolecular complexes have been reported to show potential photothermal properties due to their narrow energy gap to enhance non-radiative decay.[61–65] The effect of the donors or acceptors as molecular motors on the supramolecular assembly has been less reported. Moreover, considering that the bond stretching vibration is an intrinsically dramatic and less restricted motion model,[58,65] it is particularly interesting to incorporate such motion into a donor or acceptor motor to further boost the photothermal conversion of the supramolecular complex.

In this work, we fabricate an electronic donor–acceptor supramolecular complex with 1,4,5,8,9,11-hexaazatriphenylenehexacarbonitrile (HAT-CN) and perylene as the acceptor and donor, respectively. Due to their apparently opposite electronic properties, the supramolecular complex can be formed readily driven by electrostatic forces. This can be confirmed by the absorption, powder X-ray diffraction (PXRD), Fourier transform infrared (FT-IR) and Raman spectral analyses of the supramolecular complex as well as the individual components. The supramolecular interaction has enabled the donor and the acceptor as a unity, where the charge transfer can occur between them in the space to induce evident NIR absorption at ~740 nm in the powder. With the complex powder, the prompt photothermal conversion by a temperature of more than 190 °C can be obtained under 808 nm laser irradiation, and this behavior is controllable and shows good stability. We also fabricate supramolecular complex-contained nanoparticles (NPs) through a nanoprecipitation method with Pluronic F127 as a matrix with their morphology, stability and biocompatibility well characterized. Inherited from the supramolecular interactions, the NIR absorption and good photothermal conversion still remain in the NPs. The photothermal conversion efficiency of the NPs is evaluated to be as high as 59.4%. The theoretical investigation reveals that the extremely strong electron affinity of the acceptor can remarkably narrow the energy gap in the complex to facilitate the photothermal conversion. More interestingly, the bond stretching vibration is dramatic and sufficient in the acceptor, enabling it as an acceptor motor to tune the structural relaxation of the complex to further boost the photothermal properties. Single crystal diffraction suggests that stable supramolecular assemblies can be formed in different solvents, which are driven by the electrostatic force and assisted by the intermolecular π–π stacking effect and C–H···N hydrogen bonds. Due to the photothermal effect, good phototoxicity is proved at a cell level by the MTT assay, cell imaging and flow cytometry. The photothermal conversion can also enable thermal imaging and PA imaging with a high contrast in the tumor tissue of the living mice, which provides a reliable approach for imaging-guided therapy. Moreover, the photothermal ablation of the tumor can be well realized using the NPs with the therapeutic mechanism revealed. We also find that the immunomodulatory effect is concurrently activated during the therapeutic process, which may expand the applications of phototherapy. This work provides a facile, economical and flexible strategy for designing highly efficient NIR photothermal agents to accelerate biomedical applications.

Results and discussion

The search for reasonable electronic donors or acceptors is important to establish a supramolecular complex system. 1,4,5,8,9,11-hexaazatriphenylenehexacarbonitrile (HAT-CN) is a heterocyclic aromatic compound composed of the fusing pyrazine ring attached by six cyano groups at the peripheral

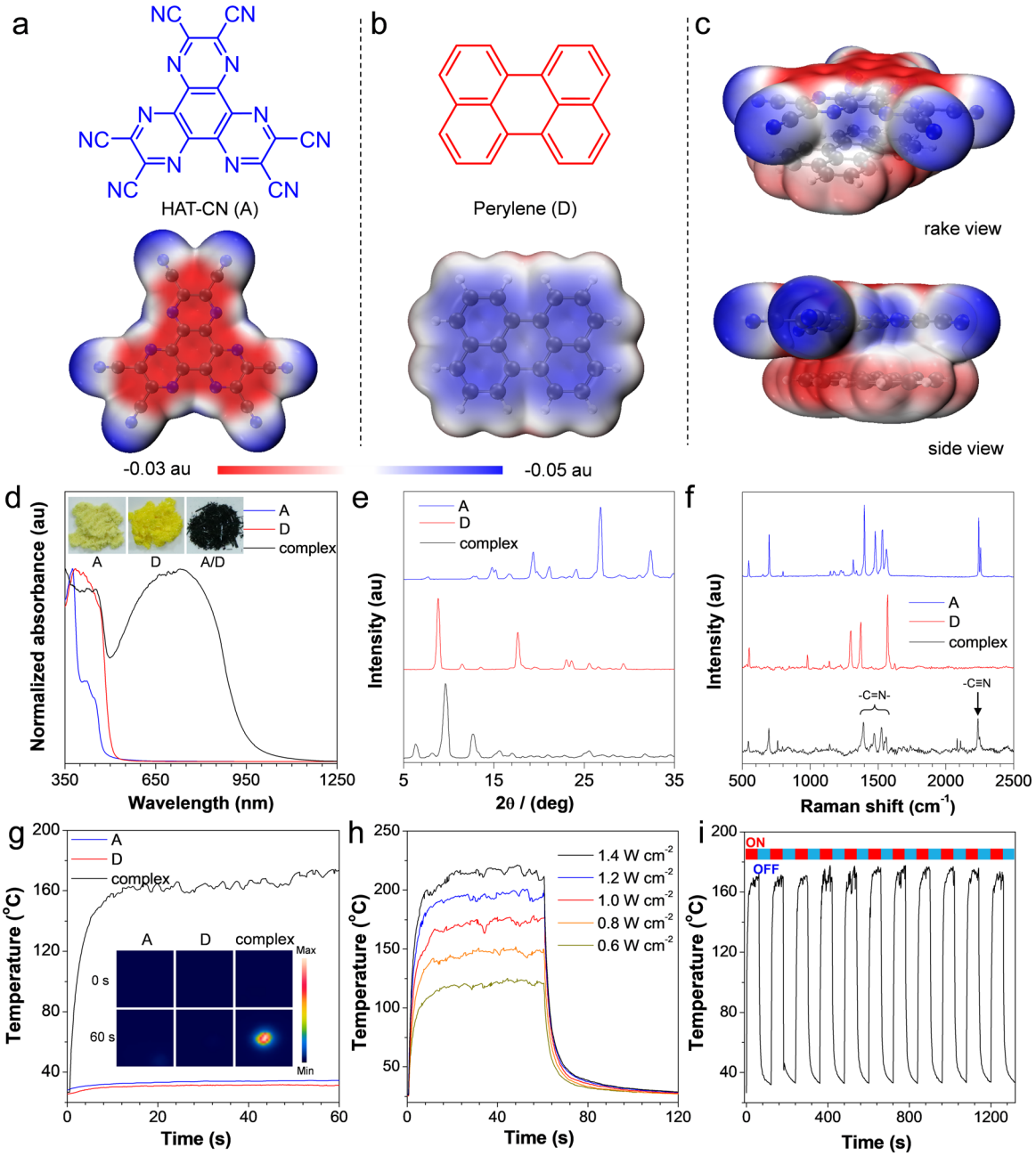

Fig. 1 Molecular structures of (a) HAT-CN and (b) perylene and their electrostatic potential surface based on optimized ground-state geometries. (c) Different views of electrostatic interaction in the D–A complex. (d) Absorption spectra of A, D and the complex in the crystalline powders. (Inset) Their photographs taken under room light. (e) PXRD diffractograms and (f) Raman spectra of A, D and complex powders. (g) Photothermal curves of A, D and complex powders under persistent 1-minute laser irradiation (808 nm, 1.0 W cm^{-2}). (Inset) Their thermal images at different time intervals. (h) Dependence of photothermal properties on the laser power density. (i) Photothermal stability during 11 heating–cooling cycles.

(Fig. 1a). The strong electron-withdrawing ability of the nitrogen heterocycle as well as the cyano groups endows it with a very strong electron affinity. Assisted by a large planar structure to facilitate π–π packing in the aggregate state, it is most commonly used as a hole-injection layer or charge-generation layer in organic light-emitting diodes.[66] The utility of HAT-CN for developing an electronic donor–acceptor supramolecular complex has been less reported. Moreover, perylene is one of the most used conjugated molecules or intermediates in organic optoelectronic materials, and it possesses electron-rich properties due to the good delocalization effect of the π electrons (Fig. 1b). Thus, using HAT-CN and perylene as the acceptor (A) and donor (D) to construct a donor–acceptor (D–A) pair or complex is viable. This is supported by our theoretical calculation (Fig. 1a–c). For example, the electrostatic potential surface of the acceptor reveals an evident electron-deficient

region at the central plane, while a relatively electropositive effect can be observed in the donor. This will facilitate the formation of a D–A supramolecular complex through a face-to-face packing of their planes by an electrostatic force. On the other hand, previous reports reveal that C–N bond stretching vibration is favorable to transform excited-state energy into heat in nitrogen heterocyclic organic dyes, while such motion is vigorous and less restricted by external factors.[58,65] We thus conceive that an acceptor containing such a structural component can act as a molecular motor in the D–A complex to further affect its properties.

We try to form the supramolecular complex by cocrystal growth from the acceptor/donor solution (molar ratio = 1 : 1) with acetone as a solvent. Fortunately, after evaporation of the solvent, a black crystal-like powder can be obtained readily, which is much different from the individual components with a yellow or pale-yellow color (Fig. 1d). The absorption spectra suggest that the absorption maxima of the acceptor and donor powders are at 374 nm and 450 nm, respectively, while remarkably red shifted absorption at ~740 nm can be observed in their complex powder. This is in consistent with previous studies, which show that through-space charge transfer occurs between the acceptor and donor due to the supramolecular interaction. Moreover, the evident allochroic effect after the complexation implies that such supramolecular interaction can be visualized by the naked eye. The crystallinity of complex powder is further investigated by powder X-ray diffraction (PXRD) (Fig. 1e). The PXRD diffractograms show that all these powders are highly crystalline, and the diffraction peaks from the complex powder are apparently different from those of the individual components, suggesting that the cocrystals are formed with a different packing model between the acceptors and donors in the aggregate state when compared with the individual components. From the Fourier transform infrared (FT-IR) spectra (Fig. S1), it is obvious that the stretching vibration of –C–H bonds only existing in the donor exhibits a signal at 3045 cm^{-1}, which shifts to 3049 cm^{-1} in the complex. Besides, the absorption peaks at 1558 cm^{-1} and 1340 cm^{-1} are assigned to the stretching vibrations from –C=N and –C–N– bonds in the acceptor,[67] which are blue-shifted by ~8 cm^{-1} and 3 cm^{-1}, respectively, after the complexation. This is due to the enhanced electron communication from the donor to the acceptor decided by the supramolecular interactions. The Raman spectra suggest that the signals from –C≡N and –C=N– bonds in the acceptor have a negative shift by 3–8 cm^{-1} in comparison to that in the complex, further confirming that the charge distribution between the donor and acceptor has been adjusted due to the supramolecular interactions (Fig. 1f).[68]

Considering the evident NIR absorption of the donor–acceptor complex caused by the supramolecular interaction, we next investigate whether the photothermal effect could be realized in this system. To confirm it, 15 mg of the cocrystal powder is placed on the glass substance and shaped into a circle (1.0 cm^{-2}), followed by irradiating it with an 808 nm laser (1.0 W cm^{-2}) (Fig. 1g). The results indicate that after laser irradiation, the temperature of the cocrystal powder rises sharply within 10 s and almost remains constant afterwards. Compared with the powder in the dark, a prompt temperature elevation by 147 °C has been realized after light irradiation. In contrast, nearly no photothermal behavior can be observed in the individual components under the same conditions, mostly because they lack absorption in the NIR region. The thermal images also suggest that a remarkable heating effect can be obtained solely in the complex powder under persistent laser irradiation. The dependence of photothermal behavior on the laser power is further evaluated (Fig. 1h). It is clear that increasing the laser power has a positive effect on the heating rate and a maximum heating effect by more than 190 °C can be recorded at a power density of 1.4 W cm^{-2}. Moreover, the photothermal stability of the complex is investigated using a persistent heating–cooling experiment (Fig. 1i). It shows that even after 11 heating–cooling cycles, the photothermal performance of the complex still changes less, suggesting that the complex stabilized by the supramolecular interaction shows good stability under light irradiation and heat stimulation. The excellent photothermal conversion, controllable photothermal effect and good photothermal stability make it an ideal photothermal material for further applications.

To reveal the cause for the photothermal effect, the theoretical simulation of the donor–acceptor complex as well as their individual components is performed. It is clear that the highest occupied molecular orbital (HOMO) and lowest unoccupied molecular orbital (LUMO) of the donor and acceptor almost occupy the whole molecular skeletons based on the optimized S_0 conformations, suggesting local-state transition properties (Fig. 2a). However, in the supramolecular complex, an obvious charge transfer has occurred from the donor to the acceptor in the space. It is due to the different electronic properties of the donor and acceptor and the supramolecular interaction has impelled them as a unity where the frontier molecular orbitals are redistributed. The energy gap of the complex is thus reduced remarkably to benefit the heat conversion because according to the energy gap law, the non-radiative decay is monotonically exponentially increased as the energy gap narrows. Besides, the structural relaxation of the donor or acceptor in the complex will play another important role in heat generation after light excitation. This can be reflected by the reorganization energy (λ) determined using the MOMAP package.[69–71] The results indicate that the total λ values of the D–A pair in the gas phase and aggregate state are 5572 cm^{-1} and 5369 cm^{-1}, respectively (Fig. 2b and c). This suggests the molecular motions after the light excitation are vigorous as reflected by a large λ while such motions are less restricted by the aggregation. From the plots of λ *versus* normal frequencies, the high frequency vibration modes corresponding to the bond length variation or bond stretching vibration are evidently stronger than the lower frequency vibration modes in both the gas phase and the aggregate state. Casting λ onto the internal coordinate manifests that the contribution of the bond stretching vibration to the total λ is more than 70% in both states, which is much higher than that from the changes in the bond angle and dihedral angle (Fig. 2b and c). Thus, the structural relaxation of the D–A complex is mainly managed by the interior bond stretching vibration. As the bond stretching

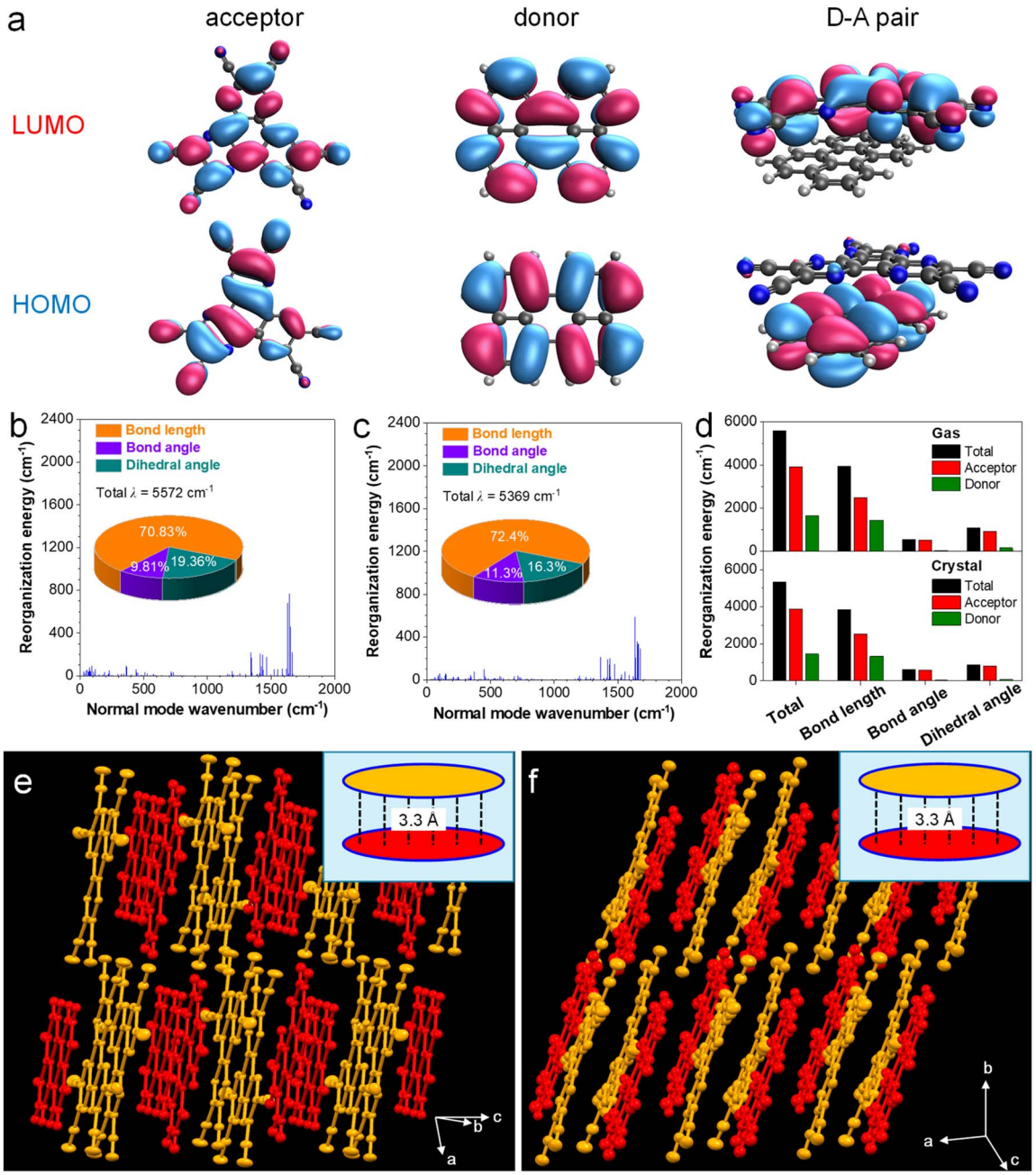

Fig. 2 (a) Frontier molecular orbitals (HOMO and LUMO) based on the ground-state geometries of A, D and the D–A pair. Reorganization energy (λ) *versus* wavenumber of the D–A pair in the (b) gas phase and (c) crystal state. (Inset) Contributions of bond length, bond angle and dihedral angle to total λ. (d) Contributions of bond length, bond angle and dihedral angle variations from the acceptor and donor in the D–A pair. Intermolecular packing models of the cocrystals grown in (e) acetone (CCDC 2414436) and (f) 1,2-dichloroethane (CCDC 2414437). (Inset) The $\pi-\pi$ interactions in the D–A pair.

vibration always takes place within a short distance, it is minimally affected by the external environment, enabling the supramolecular complex to achieve efficient photothermal conversion.

Interestingly, we find that whether in the gas phase or the aggregate state, most of the contribution to molecular relaxation in the supramolecular complex originates from the acceptor. This is evidenced by their large λ proportions of 70.5% and 72.9% from the total (Fig. 2d). More specifically, the bond stretching vibration has dominated the structural relaxation in the acceptor in comparison to the other motions such as the changes in the bond angle and dihedral angle, and such a motion is almost from the central fusing pyrazine ring. Note that the variation in the dihedral angles mainly originates from the rotation of the cyano groups against the central plane and the twist of the plane, while those motions can be suppressed from the gas phase to the aggregate state due to their sensitivity to the external environment. This may give rise to a weak change

of the total λ between two states due to the small contribution. The large λ proportions from the acceptor in the supramolecular complex and the bond stretching vibration in the acceptor suggest that the acceptor can function as a molecular motor to drive the conformational relaxation in the supramolecular complex to promote the photothermal conversion, while the motion is governed by the dramatic and less restricted bond stretching vibration.

The possibility of the conformational change of the donor or acceptor is also investigated by experimental analysis. As revealed by the UV-vis and fluorescence spectra, the absorption and emission of the perylene are almost mirror-symmetric with a fine structure (Fig. S2). They have an obvious overlap in the spectra with a very small Stokes shift. This suggests that the structure of the perylene is very rigid and hard to relax after being pumped to the excited state. In stark contrast, although the structure of HAT-CN seems to be rigid due to its good planarity, a large Stokes shift by ~80 nm and structureless peaks can be found in their spectra (Fig. S3). Therefore, a dramatic molecular motion without the obvious conformational change can take place in the interior of the acceptor. It matches well with our concept that the bond stretching vibration-manipulated acceptor motor would play a major role in the conformation relaxation of the supramolecular assembly after the light excitation. Moreover, the supramolecular complex of TCNQ-perylene with the same donor was reported,[63] while its photothermal conversion efficiency is much worse than that of the HAT-CN-perylene complex even though it possesses a reduced energy gap to boost the photothermal effect. It suggests that the molecular motions involved in HAT-CN but lost in the TCNQ play an important role in enhancing the photothermal performance of the supramolecular complex.

We also study the crystal structure of a D–A cocrystal grown in the acetone, which may provide a deeper insight into the supramolecular self-assembled structure (Fig. 2e). The results indicate that the donor and acceptor adopt a mixed staking fashion while they alternate in the plane direction in the aggregate state. Due to the good planarity of the donor and acceptor, a dense and well packing between them can be obtained with a short distance of 3.3 Å, which is induced by the electrostatic interaction and the π–π stacking effect. Besides, we also find other intermolecular interactions that may assist the self-assembly process. For example, the cyano groups in the acceptor provide rich nitrogen sites to bind with the hydrogen atoms in the adjacent donor through a hydrogen bond interaction (Fig. S4). These multiple C–H···N hydrogen bonds are found in a range from 2.54 to 3.28 Å, which can serve as a favorable factor to stabilize the assembled structure. To prove the universality of utilizing HAT-CN and perylene as the acceptor and donor to construct the D–A supramolecular complex, the cocrystal growth is performed in a different solvent of 1,2-dichloroethane. In this case, the cocrystal is still easy to form (Fig. 2F). Although the relative orientation between the donor and acceptor has changed slightly, the packing model and distance are almost the same as those formed in acetone. Moreover, the strong intermolecular hydrogen bonds also prevail between the donor and acceptor to fix the assemblies (Fig. S5). All these suggest that the stable donor–acceptor supramolecular complexes are readily formed as driven by electrostatic force while assisted by the intermolecular π–π stacking effect and C–H···N hydrogen bonds.

To benefit biomedical applications, we fabricate D–A complex nanoparticles (NPs) *via* a nanoprecipitation method with Pluronic F127 as a matrix (Fig. 3a). The NPs can be readily formed and they show crystallinity with the PXRD diffractogram similar to that of the complex powder (Fig. S6). After further filtration, NPs with a diameter of ~130 nm and narrow distribution can be observed by dynamic light scattering (DLS) (Fig. 3b). The transmission electron microscopy (TEM) image shows that they are spherical with a size close to the observation from DLS (Fig. 3b). The UV-vis spectrum reveals that they possess an obvious NIR absorption in a range from 700 nm to 1050 nm with an absorption maximum at ~840 nm (Fig. 3c), which is due to the through-space charge transfer in the supramolecular complex. The photograph of the NP aqueous solution taken under room light shows that they are deep green and well dispersed in the water without any precipitate (Fig. 3c). The stability of the NPs is further investigated using the DLS and UV-vis spectra during two-week storage. The results show that negligible changes can be found both in the particle size and absorption intensity, suggestive of good morphological and colloidal stability of the NPs (Fig. 3d and S7).

The photothermal properties of the NPs are further evaluated. Upon 808 nm laser irradiation (1.0 W cm^{-2}), the temperature of the NPs rises rapidly in 8 minutes and increasing the NP concentration exerts a positive effect on the photothermal conversion (Fig. 3e). As a control, nearly no temperature change can be observable in water under the same irradiation conditions. Besides, the photothermal behavior of the NPs is also related to the laser power and a higher laser power may lead to a quick heating rate (Fig. 3f). The photothermal stability of NPs is proved to be pretty good as reflected by a smaller loss in the performance after the repeated heating–cooling experiment (Fig. 3g). The photothermal conversion efficiency of the NPs is determined to be 59.4% based on the reported method (Fig. S8),[57] which is higher than that of nanomaterials built from other donor–acceptor supramolecular complexes,[62,63,72] and most organic and inorganic materials (Table S1). This implies that the through-space charge transfer as well as the acceptor motor can collectively contribute to a high photothermal conversion efficiency. Thanks to such good properties, a distinct photoacoustic signal peaking at ~825 nm can be generated under the laser excitation (Fig. 3h). The PA signal is similar to the absorption profile of the NPs and it cannot be detected in the presence of water. This confirms that the PA signal originates from the complex in the NPs with a charge transfer effect. The PA stability is studied under persistent laser irradiation and the PA intensity remains at ~90% after 8-minute irradiation, suggestive of good PA stability (Fig. 3i). Moreover, the PA intensity is enhanced with an increase of the NP concentration and a good linear relationship with a correlation coefficient of 0.9952 can be obtained (Fig. 3i). This suggests that it is suitable for a quantitative analysis based on the PA intensity of the complexed NPs.

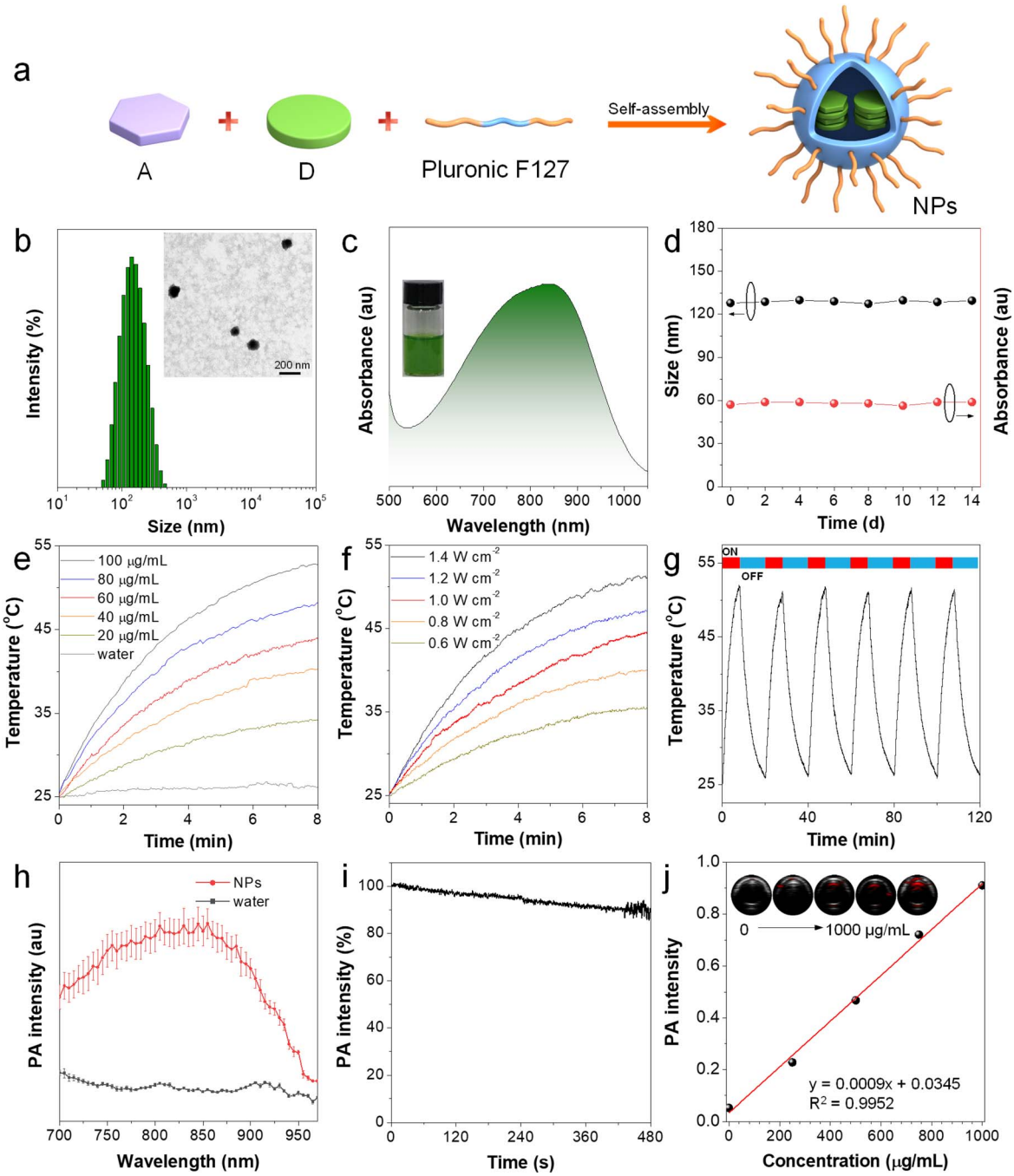

Fig. 3 (a) Route to fabricate complex-containing NPs. (b) DLS of NPs in water. (Inset) Their TEM image. (c) UV-vis spectrum of NPs in water. (Inset) Their photographs taken under room light. (d) Particle sizes and absorption intensities of NPs during two-week storage. (e) Photothermal curves of NPs under 808 nm laser irradiation (1.0 W cm^{-2}) at different concentrations. (f) Photothermal curves of NPs at different irradiation power densities. (g) Photothermal stability of NPs during 6 heating–cooling cycles. (h) PA spectra of NPs and water. (i) PA stability of NPs for 8 minutes. (j) Dependence of PA intensities on the NP concentrations. (Inset) The PA images at different concentrations.

Then, the phototherapeutic properties of the NPs are evaluated at a cell level. The photo-toxicity of the NPs is studied using a MTT assay based on CT26 cells. Prior to this, the biotoxicity of the individual components is evaluated both in the absence and in the presence of laser irradiation (808 nm, 1.0 cm^{-2}), and both of them show negligible toxicity in a wide concentration range under these conditions (Fig. 4a and b). After complexation into the NPs, their dark toxicity can still be ignored (Fig. 4c). However, under laser irradiation, the cell death increases dramatically with an increase of the NP concentration and almost 80% of the cells have been killed when the concentration reaches 60 μg mL^{-1}. This suggests that the NPs as well as their components show good cell biosafety in the absence of light, and only superior phototoxicity can be activated after

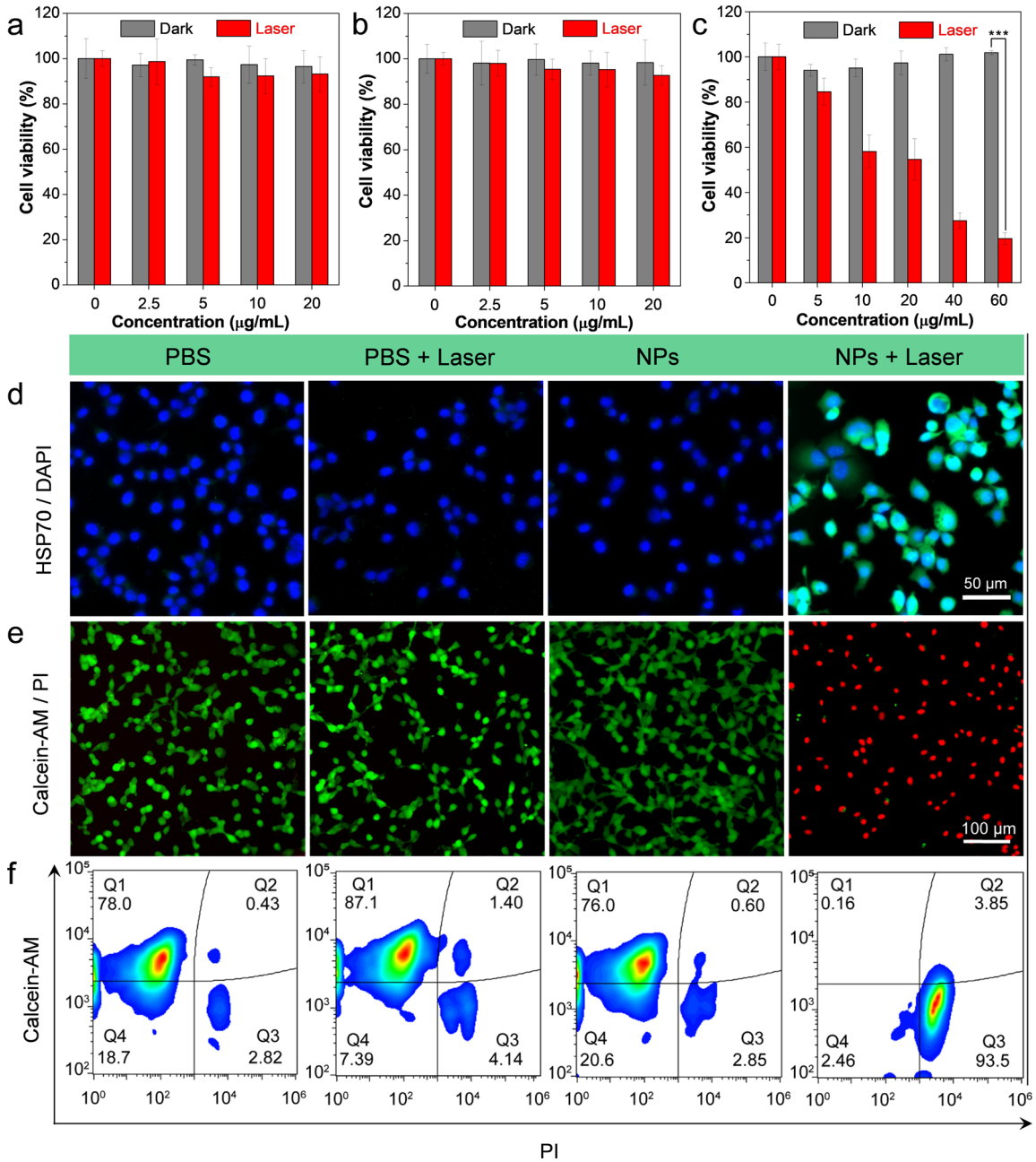

Fig. 4 Cell viability of CT26 cells after treatment with (a) A, (b) D and (c) NPs with different concentrations. (d) Cell imaging showing the HSP70 expression in CT26 cells after different treatments. The cell nuclei were stained with DAPI. Scale bar: 50 μm. (e) Fluorescence microscopy of live/dead staining of CT26 cells after different treatments with calcein-AM and PI as indicators. Scale bar: 100 μm. (f) Flow cytometry analysis of live/dead staining of CT26 after different treatments.

supramolecular complexation between the donor and acceptor. Moreover, the photothermal immune effect from the NPs is studied by an express of tumor-specific antigen HSP70 in the cells (Fig. 4d).[73] As divided the cells into four groups namely PBS, PBS + Laser, NPs, NPs + Laser, respectively, the immunofluorescence express of HSP70 protein can be remarkably enhanced in the group treated with both NPs and the laser irradiation. Moreover, to visually evaluate the cytotoxicity, calcein acetoxymethyl ester (calcein-AM) and propidium iodide (PI) are separately utilized for fluorescence staining of live and dead cells (Fig. 4e). The results indicate that in the groups of PBS, PBS + Laser and NPs, only the green fluorescence signal from calcein-AM can be observed, suggesting that they are safe and intact after these treatments. In contrast, in the NPs + Laser group, almost all of the cells are dead as reflected by a distinct red fluorescence signal from the PI. To conduct a further quantitative analysis of the cell viability and death, the cells in each group after the treatments are investigated by flow cytometry (Fig. 4f). The results suggest that a high death rate of CT26 cells can be found only in the NPs + Laser group, with

93.8% of the cells eliminated by the photothermal effect (Fig. S9).

To further assess the *in vivo* imaging and therapeutic effects of the NPs, a CT26 tumor model was established in BALB/c mice. The CT26 tumor bearing mice are randomly divided into four groups ($n = 5$): treated with PBS, PBS + Laser (L), NPs and NPs + Laser (L), respectively, while the PBS and NPs are injected intratumorally into the tumor tissues (Fig. 5a). Due to the good photothermal properties of the NPs, their photothermal effect in the tumor tissues is evaluated after injection of the NPs by 2 h. It shows that there is almost no thermal signal in the tumor before the laser irradiation (808 nm, 1.0 cm^{-2}) (Fig. 5b). However, after the laser irradiation, the heating effect appears, and the signal intensity enhances gradually with time and almost remains constant after 5 minutes (Fig. 5b and c). Under the same conditions, the control group without injection of the NPs shows a weak thermal imaging signal (Fig. 5c and S10). This suggests that the photothermal conversion from the NPs upon the light excitation can work pleasantly in the tumor to provide a distinct thermal imaging signal. Moreover, as the PA signal is caused by the thermal-elastic expansion effect, their PA imaging performance in the tumor is investigated. The results suggest that there is a weak PA signal in the tumor tissue before the administration of the NPs (Fig. 5d), which originates from the

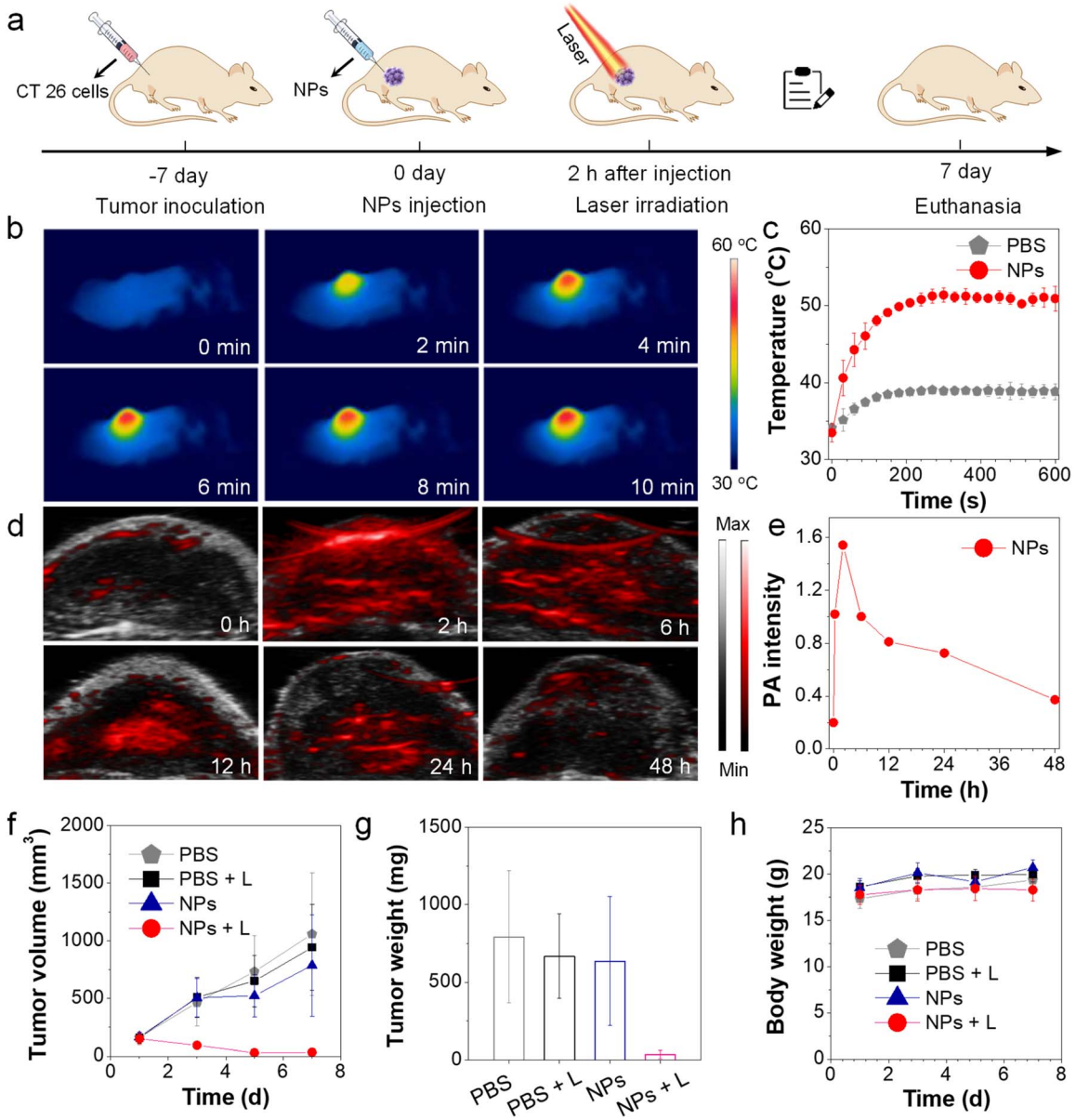

Fig. 5 (a) Schematic illustration of the construction of the CT26 tumor mouse model and evaluation of imaging-guided phototherapy with the NPs. (b) Thermal imaging of CT26 tumor-bearing mice irradiated with an 808 nm laser at different time intervals after injection of the NPs by 2 h. (c) Changes of temperature *versus* time in mice treated with the NPs and PBS. (d) PA images of CT26 tumor-bearing mice at different time intervals after injection of the NPs. (e) Changes of PA intensity *versus* time. Changes in (f) tumor volume, (g) tumor weight, and (h) mouse body weight with different treatments at the end of the efficacy assessment.

absorption in the biological substrates such as endogenous melanin and hemoglobin. After the administration of the NPs, the PA intensity rises dramatically with time and reaches a maximum at 2 h, which is probably due to quick diffusion and enhanced dispersion of the NPs in the tumor tissue (Fig. 5d and e). After that, the PA signal declines gradually with only a weak signal left at 48 h. This is due to decreased accumulation of the NPs in the tumor tissue caused by the good metabolism effect of the NPs. It is noteworthy that a notable PA signal enhancement by more than 7.5-fold can be found at the peak intensity indicative of a good signal-to-noise ratio in the practical imaging application (Fig. 5e). Together with the concentration-dependent PA effect, the NPs are particularly useful in further imaging-guided photothermal therapy.

Then, the therapeutic effect caused by the photothermal effect from the NPs is also evaluated. During the treatment period, the tumor volume and the body weight of the mice in each group are monitored every two days. It is clear that in the group treated with the NPs plus laser irradiation (808 nm, 1.0 W cm^{-2}), the tumor volume reduces rapidly with time while the tumors are almost removed on day 7, suggesting a good therapeutic efficacy towards the tumor treatment, which is in good agreement with the *in vitro* phototoxicity studies (Fig. 5f). As controls, the tumors in the other groups show an evident increase in the sizes due to the lack of the photothermal effect. The evaluation of the tumor weight on day 7 confirms that only a small portion of the tumor remains in the NPs + Laser group and a sharp difference can be found between the groups with

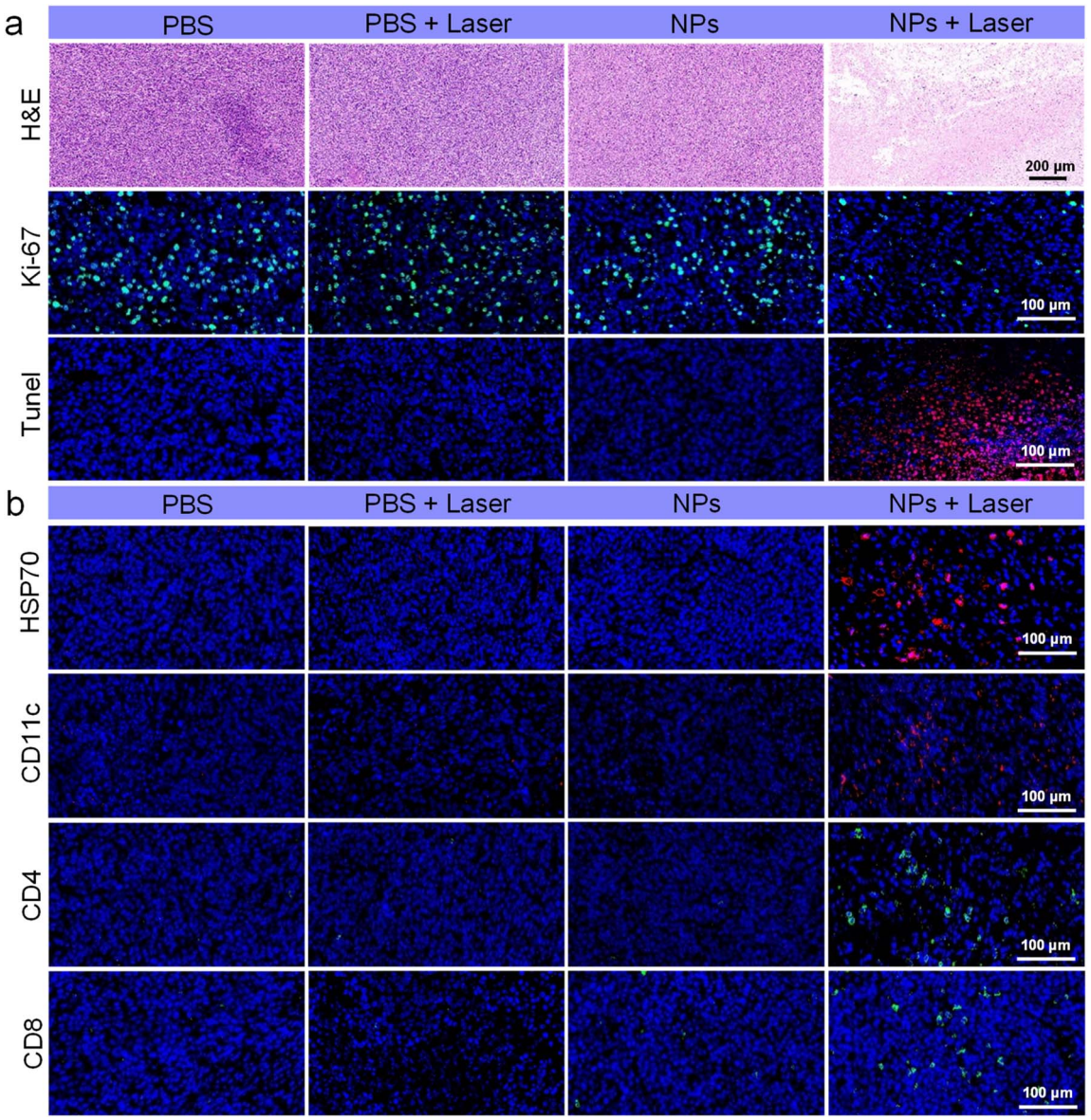

Fig. 6 (a) Representative H&E, Ki-67 and TUNEL staining images of tumor tissues from mice in different treatment groups. Scale bars for H&E, Ki-67 and TUNEL staining are 200 μm, 100 μm and100 μm, respectively. (b) Representative images of immunofluorescence staining of HSP70, DC cells (CD11c) and T cells (CD4 and CD8) expression after different treatments. Scale bar: 100 μm.

and without the photothermal therapy (Fig. 5g). However, throughout the treatment process, the body weight of the mice in all groups shows a negligible change, suggesting that their growth behavior is less influenced by the phototherapy (Fig. 5h). Moreover, the anti-tumor mechanism in terms of cancer cell death is investigated using pathological scrutiny based on the extracted tumor tissue slices. The cell morphological characteristics, cell proliferation level and apoptotic event of the tumor are evaluated by hematoxylin and eosin (H&E) staining, expression of proliferative marker (Ki-67) staining and terminal-deoxynucleotidyl transferase uridine triphosphate adenine end labeling (TUNEL) staining, respectively (Fig. 6a). Notably, the tumor cells in the NPs + Laser group show significant damage as reflected by the blurry cell boundary and the loss of the cell nucleus. This is in sharp contrast to the control groups, which display distinct and normal cell morphologies. Moreover, by comparison to the controls, the NPs + Laser group exhibits an evident decrease in the expression of the Ki-67 signal and an increase in the TUNEL signal, suggesting that the photothermal effect has led to prominent cell apoptosis while the cell proliferation is effectively suppressed. All these suggest that with our supramolecular complex, the efficacious photothermy can be generated to photoablation of the tumors.

To further clarify the mechanism underlying the thermotherapy induced by the NPs, immunofluorescence assays are carried out (Fig. 6b). These experiments provide solid evidence that in the NPs + Laser group, the generated photothermal effect can evoke the release of the heat shock protein (HSP70) from the tumor cells as evidenced by its marker and give rise to an increase in the number of dendritic cells (DC cells) and T cells as proved by the CD11c, CD4 and CD8 markers. This finding verifies that the employment of the NPs for thermotherapy can facilitate the liberation of HSP70 from the tumor cells, which in turn contributes to the enhanced local infiltration of antigen-presenting cells (APCs) and T cells into the tumor tissues, thereby realizing an immunomodulatory effect.[74] Thus, the photothermal effect from the supramolecular complex can cause effective thermotherapy to eradicate the *in situ* tumor cells and meanwhile trigger a systemic immune response, which serves as a promising approach for further development of an efficacious tumor treatment strategy.

Finally, the biosafety of the NPs is evaluated because it is a key factor in the practical biomedical application. After the different treatments on day 7, the mice are euthanized and their blood samples are collected for routine blood as well as the liver and kidney function analyses (Tables S2 and S3). The indices corresponding to each item show that there are few differences between the experimental and control groups, and they are all in a normal range. Moreover, the major organs (including heart, liver, spleen, lung and kidney) of the mice are extracted and their slices are studied by H&E staining (Fig. S11). The results indicate that distinct cell morphologies are observable from each organ with minimal differences observed between the different groups. The blood test and the histological examination confirm that the NPs constructed from the supramolecular complex possess good biocompatibility.

Conclusions

In this work, for the development of a NIR photothermal agent for biomedical applications, an electronic donor–acceptor supramolecular assembly is established based on the complexation of HAT-CN and perylene as the acceptor and donor, respectively. The supramolecular interaction in the D–A complex is proved by absorption, PXRD, FT-IR and Raman spectroscopies. The single crystal diffraction of the cocrystals formed in acetone and 1,2-dichloroethane suggests that the supramolecular complexation is driven by the electrostatic force due to the opposite electronic properties of the planar donor and acceptor and assisted by the intermolecular π–π stacking effect and C–H···N hydrogen bonds. It is revealed that these favorable interactions can lead to a similar and stable self-assembled structure irrespective of the solvents. Different from the local-state transition in the donor or acceptor, an obvious charge transfer can occur from the donor to the acceptor in the supramolecular complex in the space, which induces distinct NIR absorption in the crystalline powder as well as the NPs. Further studies indicate that under the excitation of a NIR laser (808 nm, 1.0 W cm^{-2}), an evident photothermal effect can be achieved. The photothermal properties of the complex are tunable and show good stability. We find that a maximum heating effect by more than 190 °C is obtained in the powder and the photothermal conversion efficiency of the NPs reaches as high as 59.4%. Theoretical investigation reveals that the narrowed energy gap caused by the through-space charge transfer can facilitate nonradiative decay to generate heat. More interestingly, HAT-CN can act as an acceptor motor in the supramolecular complex, while in the interior the dramatic bond stretching vibration plays a key role in the structural relaxation of the complex to further boost the photothermal conversion. Due to the good photothermal properties, the NPs possess excellent phototoxicity towards CT26 cells as revealed by the MTT assay, cell imaging and flow cytometry. Moreover, with the NPs, the *in vitro* PA properties and *in vivo* PA imaging based on the CT26 tumor bearing mice are proved to be pretty good. Guided by the PA imaging, the effective photoablation of the tumor can be achieved with the therapeutic effect studied by pathological scrutiny. Further studies using immunofluorescence assays indicate that the photothermal immunomodulatory effect is concurrently activated, which may enhance the therapeutic effect. Finally, the good biocompatibility of the NPs is proved at the cellular and tissular levels and by blood analysis. Our study provides a facile, economical and flexible strategy to generate a highly efficient NIR agent for photothermal therapy by the merging of the electronic donor–acceptor supramolecular complex and the light-driven molecular motor.

Ethical statement

All animal procedures were performed in accordance with the Guidelines for Care and Use of Laboratory Animals of Guangzhou Medical University and approved by the Animal Ethics Committee of Guangzhou Medical University, GY2024-587.

Author contributions

Y. L., M. C. and B. Z. T. conceived and designed the experiment. C. Z. prepared the complex and studied the properties. L. Z. conducted the biological experiment. J. Z. conducted the theoretical calculation. X. Deng determined the photothermal conversion of the nanoparticles. Z. Z. and X. He studied the morphology and stability of the nanoparticles. M. M. analyzed the single crystal structure. Q. Z., J. L. and J. W. Y. Lam provided suggestions during the study. Y. L. and M. C. analyzed the data and co-wrote the paper. All authors approved the final version of the manuscript.

Conflicts of interest

There are no conflicts to declare.

Data availability

CCDC 2414436 and 2414437 contain the supplementary crystallographic data for this paper.[75a,b]

The data supporting this article have been included in the main text and part of the supplementary information (SI). Supplementary information is available. See DOI: **https://doi.org/10.1039/d5sc05770a**.

Acknowledgements

This work is partially supported by the National Natural Science Foundation of China (22275072 and 22275040), the Project of Science and Technology of Guangzhou (2024A04J3712), the Guangdong Basic and Applied Basic Research Foundation (2023A1515110808), the Key-Area Research and Development Program of Guangdong Province (2024B0101040001), the Shenzhen Key Laboratory of Functional Aggregate Materials (ZDSYS20211021111400001), and the Science Technology Innovation Commission of Shenzhen Municipality (KQTD20210811090142053).

References

1 J.-M. Lehn, *Angew. Chem., Int. Ed.*, 1988, **27**, 89–112.
2 J.-M. Lehn, *Chem. Soc. Rev.*, 2017, **46**, 2378–2379.
3 J. Zhou, L. Rao, G. Yu, T. R. Cook, X. Chen and F. Huang, *Chem. Soc. Rev.*, 2021, **50**, 2839–2891.
4 Y. Li, F. Huang, P. J. Stang and S. Yin, *Acc. Chem. Res.*, 2024, **57**, 1174–1187.
5 L. Yang, X. Tian, Z. Wang and X. Zhang, *Chem. Rev.*, 2015, **115**, 7196–7239.
6 C. Guo, A. C. Dedgwick, T. Hirao and J. L. Sessler, *Coord. Chem. Rev.*, 2021, **427**, 213560.
7 L. C. Gilday, S. W. Robinson, T. A. Barendt, M. J. Langton, B. R. Mullaney and P. D. Beer, *Chem. Rev.*, 2015, **115**, 7118–7195.
8 J. Zheng, Z. Lu, K. Wu, G.-H. Ning and D. Li, *Chem. Rev.*, 2020, **120**, 9675–9742.
9 H.-T. Feng, J. W. Y. Lam and B. Z. Tang, *Coord. Chem. Rev.*, 2020, **406**, 213142.
10 S. Ji, M. Zeng, X. Zhan, H. Liu, Y. Zhou, K. Wang, Y. Yan, J. Yao and Y. S. Zhao, *J. Am. Chem. Soc.*, 2024, **146**, 22583–22589.
11 L. Sun, Y. Wang, F. Yang, X. Zhang and W. Hu, *Adv. Mater.*, 2019, **31**, 1902328.
12 Y. Sun, Y. Lei, H. Dong, Y. Zhen and W. Hu, *J. Am. Chem. Soc.*, 2018, **140**, 6181–6189.
13 S. K. Park, J. H. Kim and S. Y. Park, *Adv. Mater.*, 2018, **30**, 1704759.
14 J. Han, D. Yang, X. Jin, Y. Jiang, M. Liu and P. Duan, *Angew. Chem.*, 2019, **131**, 7087–7093.
15 S. Sun, J. Pang, S. Ni, G. Zhang, L. Xu, L. Dang and M.-D. Li, *J. Phys. Chem. C*, 2020, **124**(32), 17744–17751.
16 B. Huang, L. Mao, X. Shi and H.-B. Yang, *Chem. Sci.*, 2021, **12**, 13648–13663.
17 M. Madhu, R. Ramakrishnan, V. Vijay and M. Hariharan, *Chem. Rev.*, 2021, **121**, 8234–8284.
18 S. Horiuchi, K. Kobayashi, R. Kumai, N. Minami, F. Kagawa and Y. Tokura, *Nat. Commun.*, 2015, **6**, 7469.
19 J. K. Jeszka, J. Ulański and M. Kryszewski, *Nature*, 1981, **289**, 390–391.
20 P. Yu, Y. Zhen, H. Dong and W. Hu, *Chem*, 2019, **5**, 2814–2853.
21 M. Kumar, K. V. Rao and S. J. George, *Phys. Chem. Chem. Phys.*, 2014, **16**, 1300–1313.
22 M. Nakamua, S. Horiuchi, F. Kagawa, N. Ogawa, T. Kurumaji, Y. Tokura and M. Kawasaki, *Nat. Commun.*, 2017, **8**, 281.
23 K. P. Goetz, D. Vermeulen, M. E. Payne, C. Kloc, L. E. McNeil and O. D. Jurchescu, *J. Mater. Chem. C*, 2014, **2**, 3065–3076.
24 Y. Takahashi, T. Hasegawa, Y. Abe, Y. Tokura, K. Nishimura and G. Saito, *Appl. Phys. Lett.*, 2005, **86**, 063504.
25 K. P. Goetz, A. Fonari, D. Vermeulen, P. Hu, H. Jiang, P. J. Diemer, J. W. Ward, M. E. Payne, C. S. Day, K. V. Coropceanu, L. E. McNeil and O. D. Jurchescu, *Nat. Commun.*, 2014, **5**, 5642.
26 Y. Wang, H. Wu and J. F. Stoddart, *Adv. Mater.*, 2022, **34**, 2105405.
27 S. Horiuchi, Y. Okimoto, R. Kumai and Y. Tokura, *Science*, 2003, **299**, 229–232.
28 W. Wang, L. Luo, P. Sheng, J. Zhang and Q. Zhang, *Chem.–Eur. J.*, 2021, **27**, 464–490.
29 D. A. Stanfied, Y. Wu, S. H. Tolbert and B. J. Schwartz, *Chem. Mater.*, 2021, **33**, 2343–2356.
30 F. Biedermann and O. A. Scherman, *J. Phys. Chem. B*, 2012, **116**(9), 2842–2849.
31 M. Guerrini, A. M. Valencia and C. Cocchi, *J. Phys. Chem. C*, 2021, **125**(38), 20821–20830.
32 Z. Guo, S. Park, J. Yoon and I. Shin, *Chem. Soc. Rev.*, 2014, **43**, 16–19.
33 D. Xu, D. Kim, Y.-Y. Zhao, C. Kim, G. Song, Q. Hu, H. Kang and J. Yoon, *Adv. Mater.*, 2024, **36**, 2402806.
34 J. Zhou, P. Jangili, S. Son, M. S. Ji, M. Won and J. S. Kim, *Adv. Mater.*, 2020, **32**, 2001945.

35 A. Sharma, P. Verwilst, M. Li, D. Ma, N. Singh, H. Yoo, Y. Kim, Y. Yang, J.-H. Zhu, H. Huang, X.-L. Hu, X.-P. He, L. Zeng, T. D. James, X. Peng, J. L. Sessler and J. S. Kim, *Chem. Rev.*, 2024, **124**, 2699–2804.
36 T. Li, J.-C. Liu, E.-P. Liu, J.-Y. Wang, P.-Y. Liao, J.-H. Jia, Y. Feng and M.-L. Tong, *Chem. Sci.*, 2024, **15**, 1692–1699.
37 Y. He, H. Liao, S. Lyu, X.-Q. Xu, Z. Li, L. McCulloch, W. Yue and Y. Wang, *Chem. Sci.*, 2021, **12**, 5177–5184.
38 S. Bian, X. Zheng, W. Liu, Z. Gao, Y. Wan, J. Li, H. Ren, W. Zhang, C.-S. Lee and P. Wang, *Biomaterials*, 2023, **303**, 122380.
39 E. Middha and B. Liu, *ACS Nano*, 2020, **14**, 9228–9242.
40 X. We, C. Xu, P. Cheng, Y. Hu, J. Liu, M. Xu, J. Huang, Y. Zhang and K. Pu, *J. Am. Chem. Soc.*, 2024, **146**, 17393–17403.
41 A. Sharma, P. Verwlist, M. Li, D. Ma, N. Singh, J. Yoo, Y. Kim, Y. Yang, J.-H. Zhu, H. Huang, X.-L. Hu, X.-P. He, L. Zeng, T. D. James, X. Peng, J. L. Sessler and J. S. Kim, *Chem. Rev.*, 2024, **124**, 2699–2804.
42 S. S. Liew, Z. Zeng, P. Cheng, S. He, C. Zhang and K. Pu, *J. Am. Chem. Soc.*, 2021, **143**, 18827–18831.
43 C. Li, M. Yao, G. Jiang, L. Feng, Y. Wu, R. Sha, Y. Li, B. Z. Tang and J. Wang, *Angew. Chem., Int. Ed.*, 2025, **64**, e202419785.
44 Y. Liang, Y. Pan, L. Chen, P. Li, M. Xu, H. Zhou, X. Lu, W. Hu, C. Yin and Q. Fan, *Angew. Chem., Int. Ed.*, 2024, **136**, e20248861.
45 Y. Song, X. Tong, Y. Han and Q.-W. Zhang, *Aggregate*, 2024, **6**, e680.
46 J. Liu, W. Zhang, C. Zhou, M. Li, X. Wang, W. Zhang, Z. Liu, L. Wu, T. D. James, P. Li and B. Tang, *J. Am. Chem. Soc.*, 2022, **144**, 13586–13599.
47 V. Gude and K. Biradha, *J. Phys. Chem. C*, 2021, **125**, 120–129.
48 K.-W. Lee, Y. Wan, Z. Huang, Q. Zhao, S. Li and C.-S. Lee, *Adv. Mater.*, 2024, **36**, 2306492.
49 Y. Liu, A. Li, S. Xu, W. Xu, Y. Liu, W. Tian and B. Xu, *Angew. Chem., Int. Ed.*, 2020, **59**, 15098–15103.
50 I. Roy, A. H. G. David, P. J. Das, D. J. Pe and J. F. Stoddart, *Chem. Soc. Rev.*, 2022, **51**, 5557–5605.
51 J.-P. Collin, C. Dietrich-Buchecker, P. Gaviña, M. C. Jimenez-Molero and J.-P. Sauvage, *Acc. Chem. Res.*, 2001, **34**, 477–487.
52 B. L. Feringa, *Angew. Chem., Int. Ed.*, 2017, **56**, 11060–11078.
53 J. Zhou and J. V. Jokerst, *Photoacoustics*, 2020, **20**, 100211.
54 Y. Mantri and J. V. Jokerst, *ACS Nano*, 2020, **14**, 9408–9422.
55 D. Zhao, L. Zhang, M. Yin, Z. He, F. Fang, M. Zhan, S. Tian, F. Meng and L. Luo, *Aggregate*, 2024, **5**, e576.
56 M. Chen, Z. Zhang, R. Lin, J. Liu, M. Xie, X. He, C. Zheng, M. Kang, X. Li, H.-T. Feng, J. W. Y. Lam, D. Wang and B. Z. Tang, *Chem. Sci.*, 2024, **15**, 6777–6788.
57 D. Xi, M. Xiao, J. Cao, L. Zhao, N. Xu, S. Long, J. Fan, K. Shao, W. Sun, X. Yan and X. Peng, *Adv. Mater.*, 2020, **32**, 1907855.
58 M. Chen, X. Zhang, J. Liu, F. Liu, R. Zhang, P. Wei, H. Feng, M. Tu, A. Qin, J. W. Y. Lam, D. Ding and B. Z. Tang, *ACS Nano*, 2020, **14**, 4265–4275.
59 L. Hu, L. Shi, T. Hu, P. Chen, T. Guo, C. Wang, R. Yang and L. Ying, *J. Mater. Chem. C*, 2023, **11**, 8985–8993.
60 S. Liu, X. Zhou, H. Zhang, H. Ou, J. W. Y. Lam, Y. Liu, L. Shi, D. Ding and B. Z. Tang, *J. Am. Chem. Soc.*, 2019, **14**, 5359–5368.
61 Y. Wang, W. Zhu, W. Du, X. Liu, X. Zhang, H. Dong and W. Hu, *Angew. Chem., Int. Ed.*, 2018, **57**, 3963–3967.
62 C. Qu, W. Na, W. Ge, H. Huang, F. Gao, L. Zhong, Y. Zhao and X. Dong, *Angew. Chem., Int. Ed.*, 2021, **60**, 8157–8163.
63 S. Tian, H. Bai, S. Li, Y. Xiao, X. Cui, X. Li, J. Tan, Z. Huang, D. Shen, W. Liu, P. Wang, B. Z. Tang and C.-S. Lee, *Angew. Chem., Int. Ed.*, 2021, **60**, 11758–11762.
64 H. Xiang, Q. Yang, Y. Gao, D. Zhu, S. Pan, T. Xu and Y. Chen, *Adv. Funct. Mater.*, 2020, **30**, 1909938.
65 R. Lin, J. Liu, W. Xu, Z. Liu, X. He, C. Zheng, M. Kang, X. Li, Z. Zhang, H.-T. Feng, J. W. Y. Lam, D. Wang, M. Chen and B. Z. Tang, *Adv. Mater.*, 2023, **35**, 2303212.
66 J. Segura, R. Juárez, M. Ramos and C. Seoane, *Chem. Soc. Rev.*, 2015, **44**, 6850–6885.
67 M. Zhang, Y. Zhao, F. Kang, W. Huang and Q. Zhang, *Adv. Funct. Mater.*, 2025, **35**, 2415186.
68 S. Liu, M. Liu, X. Li, S. Yang, Q. Miao, Q. Xu and G. Zeng, *Carbon Energy*, 2023, **5**, e303.
69 Z. Shuai and Q. Peng, *Natl. Sci. Rev.*, 2017, **4**, 224–239.
70 Z. Shuai and Q. Peng, *Phys. Rep.*, 2014, **537**, 123–156.
71 Z. Shuai, *Chin. J. Chem.*, 2020, **38**, 1223–1232.
72 X. Kong, Y. Yang, G. Wan, Q. Chen, H. Yu, B. Li and L. Wu, *Adv. Healthcare Mater.*, 2022, **11**, 2102352.
73 F. Zhou, J. Yang, Y. Zhang, M. Liu, M. L. Lang, M. Li and W. R. Chen, *Clin. Cancer Res.*, 2018, **24**, 5335–5346.
74 D. G. Millar, K. M. Garza, B. Odermatt, A. R. Elford, N. Ono, Z. Li and P. S. Ohashi, *Nat. Med.*, 2003, **9**, 1469–1476.
75 (*a*) CCDC 2414436: Experimental Crystal Structure Determination, 2025, DOI: **10.5517/ccdc.csd.cc2m1f15**; (*b*) CCDC 2414437: Experimental Crystal Structure Determination, 2025, DOI: **10.5517/ccdc.csd.cc2m1f26**.